International Forum on Aeroelasticity and Structural Dynamics
IFASD 2017
25-28 June 2017, Como - Italy

NONLINEAR AEROELASTIC STEADY SIMULATION APPLIED TO HIGHLY FLEXIBLE BLADES FOR MAV

Fausto Gill Di Vincenzo[1], Mauro Linari[1], Dr F. Mohdzawawi[2], and Dr J. Morlier[3]

[1] MSC.Software
4, Rue du Professeur Pierre Vellas
Europarc, Immeuble Jupiter, B10 - 31300 Toulouse, France
faustogill.divincenzo@mscsoftware.com

[2] Universiti Teknologi Malaysi
Faculty of Mechanical Engineering, 81310 UTM Skudai Johor, Malaysia

[3] Institut Clément Ader (ICA)
Université de Toulouse
ISAE SUPAERO-CNRS-INSA-Mines Albi-UPS, Toulouse, France

Keywords: Fluid-Structure Interaction, Nonlinear Steady-State, CFD, MAV, Highly Flexible Rotating Blades

Abstract: A novel approach is presented to perform nonlinear aeroelastic steady-state simulations of highly flexible structures such as fix wings and rotating blades. The methodology has been developed in a specific OpenFSI service available in MSC Nastran SOL 400 [1] that includes follower forces and incremental loads features to allow for accurate nonlinear steady Fluid-Structure Interaction analysis. The new service, called HSA.OpenFSI, based on the HSA Toolkit [2], has been implemented to couple MSC Nastran to SC/Tetra solver from Cradle. Six DOF spline technology is used to interpolate data between the aerodynamic and structural grids [3]. A new approach has been designed to improve the efficiency of this technology that allows to considerably reduce the time needed to create the interpolation spline matrix and the disk space to store it. A Nastran-based FEM algorithm has been developed to take care of the fluid domain deformation. The proposed approach has been validated on a flap in a duct model, where transient steady-state results are available from other approaches [4], and then preliminary results on a proprotor two-blade model of Micro Air Vehicles MAV from ISAE [5] will be presented.

1 INTRODUCTION

In a standard staggered transient Fluid-Structure Interaction (FSI) simulation Finite Element Method (FEM) and Computational Fluid Dynamics (CFD) solvers run simultaneously and exchange data at each time step and within the time step depending on the coupling strategy (explicit or implicit) [6]. This kind of simulations are computationally highly intensive and time consuming. Performing a steady-state FSI simulation rather than a transient simulation would save a lot of time to get the steady-state of a structure under aerodynamic loading. As a matter of fact, as it will be showed in this work, only a few FEM-CFD exchanges are needed for an aeroelastic system to converge to the steady-state configuration with a static solution for the structure and a steady one for the fluid solver. One of the most important advantage of that approach is that a transient simulation can be concatenated to the nonlinear static analysis using

the previous deformed configuration as the starting point for a new loading condition to predict dynamic instabilities, like flutter and gusts, or perform a frequency response, without having to recalculate the overall simulation from the beginning. The chaining concept finds other interesting applications like that one of carrying out linear perturbation analysis to investigate normal modes and natural frequencies of a pre-loaded in-flight aircraft.
When geometric and material nonlinearities are taken into account, on top of the differential stiffness modelling, the effect of follower forces should be properly described since the load is a function of the solution itself [1][7]. If the aerodynamic load does not follow the deformation of the structure and update its direction accordingly, like the aerodynamic pressure does, the structure would deform wrongly (e.g. it stretches).
On the CFD side, one of the common problems that may be encountered in those applications is the issue of negative volumes. This is often the case when the CFD solver does not update the fluid domain properly around deformable walls, like blades and wings that deform too much. This can happen when the displacement of the CFD wetted surface used to drive the fluid domain deformation are received without any relaxation factor or when the algorithm employed to deform the fluid domain is not efficient and robust enough.

Aeroelastic FEM models are often simplified models that can be made by beam and shell elements with concentrated masses with a geometry that completely differs from that one of the CFD model. An inaccurate aero-structure interpolation method between dissimilar grids would than lead to unreasonable results.

Hence there is a need to build a new solution able to couple FEM models made by any element type to CFD solvers to allow for nonlinear steady coupled simulation which takes care of all the aspects described above.

The present paper illustrates a new methodology that allows to couple MSC Nastran SOL 400 with the SC/Tetra code from Cradle. The solution allows for linear and nonlinear structures, static and transient FEM simulations (the last one here shortly presented and used for comparisons), with incremental loads and follower forces capabilities, while the CFD solver can be steady and unsteady (the second one when the structural solver is transient).

2 PROPOSED APPROACH

The proposed HSA.OpenFSI service provides an interface between MSC Nastran SOL 400 and the SC/Tetra solver to allow for nonlinear fluid structure interaction simulations. The published Application Programming Interface (API) is used to build the environment and create the interface [8]. The FEM and CFD codes execute simultaneously and exchange information through the interface during the simulation, providing a tight coupling between the two codes. Data communication is done at the interface on nodes that belong to so-called wetted surfaces, which are the surfaces where the fluid is in “contact” with the structure. The structural and CFD wetted surfaces are defined independently from each other and can differ both in shape and discretization. Dissimilar geometries can be handled since the load/displacement interpolation technology takes care of it and ensures the energy equilibrium.

2.1 Steady-state FSI workflow

While in a staggered transient FSI simulation FEM and CFD solvers exchange data at each time step, in the proposed steady-state approach it happens at a specific number N of main exchanges

here called number of loads (a number N less than then is usually large enough to reach the aeroelastic system convergence), Fig. 1 (a), and also within every main exchange if the incremental loads and follower forces capabilities are activated, Fig. 1 (b).

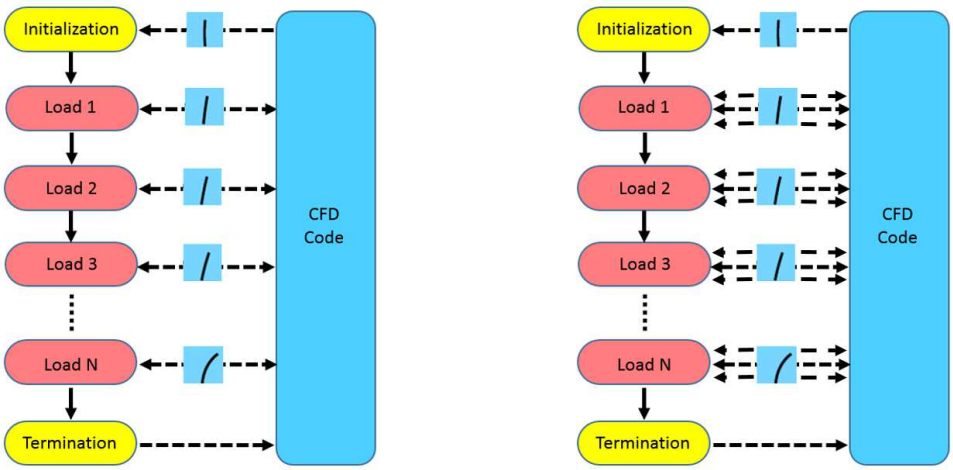

(a) Without incremental loads and follower forces (b) With incremental loads and follower forces

Fig. 1: Steady-state coupling workflow strategies

In the simplest coupling case, Fig. 1 (a), when incremental loads and follower forces capabilities are not enabled, the CFD code computes viscous and pressure forces at the beginning of the simulation. The service reads aerodynamic pressures calculated on the CFD wetted surface and transforms those into equivalent structural wetted nodal forces and moments. The aerodynamic structural loading is passed through the service to the FEM solver that computes structural displacement based on the driving forces and moments. The service interpolates back the structural displacement on the CFD wetted surface, calculates the fluid domain deformation based on the wetted surface displacement and sends the new positions of the aerodynamic grids to the CFD solver. The CFD solver updates the fluid domain, recalculates the flow field, and sends the new load to the FEM solver, Fig. 2.

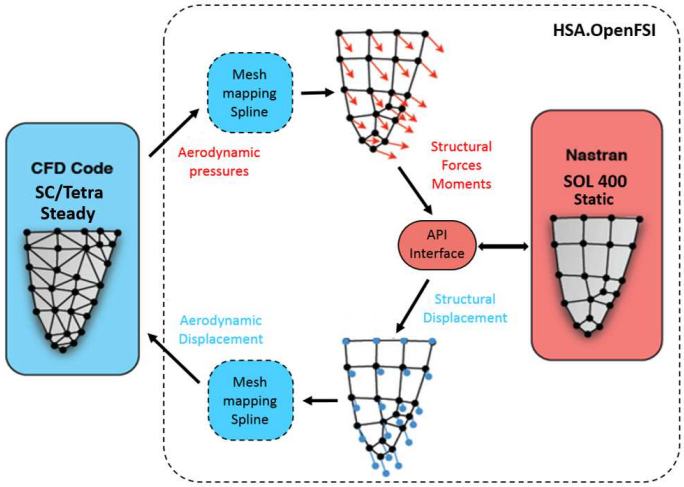

Fig. 2: Data exchange between FEM and CFD

The solution ends after N exchanges or earlier when one of the displacement/load convergence criterions is satisfied. The load convergence criterion of the aeroelastic system is defined as following:

$$\left|Load_{Grid}^{j} - Load_{Grid}^{j-1}\right| < \varepsilon_L \tag{1}$$

While the displacement one as below:

$$\left|Disp_{Grid}^{j} - Disp_{Grid}^{j-1}\right| < \varepsilon_D \tag{2}$$

In the previous equations, $Load_{Grid}^{j}$, $Load_{Grid}^{j-1}$, $Disp_{Grid}^{j}$, $Disp_{Grid}^{j-1}$, ε_L, ε_D are respectively the structural nodal forces/moments and structural displacement, evaluated on predefined grids at the exchange j and $j-1$, the load tolerance and the displacement tolerance.

The issue with such a coupling strategy, shown in Fig. 1 (a), is that the first load typically causes the most deformation of the structure with a load that would not change neither in magnitude nor in direction during the exchange, in opposition to the reality. Actually, while the structure deforms the aerodynamic load evolves and changes as well. While for linear structures such a coupling strategy could be acceptable, since small displacement and deformation, if the structure steps into the nonlinear domain, either because of material and/or geometric nonlinearities, the effect would be not negligible. Consequently, the aerodynamic displacement calculated at the end of the first exchange would produce an unreal aerodynamic shape and wrong flow field around it leading to a simulation error that would propagate through the FEM-CFD exchanges as the analysis moves forward.

2.2 Incremental loads and follower forces

To overcome the limitations explained just above, especially for those applications where structural nonlinearities are taken into account, a new coupling strategy has been designed with incremental loads and follower forces capabilities. With the incremental loads feature, within each main load exchange k, a number N_k of sub-cycles are computed between the two codes, Fig. 1(b). Instead of sending to the structure the aerodynamic load as it is, $Load_k$, the FEM solver receives it incrementally from $Load_k\ inc_1$ to $Load_k\ inc_N$ as an increasing percentage of the total load $Load_k$. The load applied to the structure at the increment $j \in [1, N_k]$, $Load_k\ inc_j$, is calculated as following:

$$Load_k\ inc_j = \frac{L_k}{N_k} * inc_j \tag{3}$$

If also the follower forces capability is activated it will be evaluated as below:

$$Load_k\ inc_j = \frac{L_k^{updated_j}}{N_k} * inc_j \tag{4}$$

In the previous equations, the quantities L_k, $L_k^{updated_j}$, N_k, and inc_j are respectively the aerodynamic load computed at the beginning of the exchange k, the aerodynamic load evaluated on the updated fluid domain at the increment j within the exchange k, the number of increments and the increment number. At every sub-cycle j the FEM solves for the structure under the load increment $Load_k\ inc_j$, interpolates the solution on the CFD grids and sends the

new displacement to the CFD solver, Fig. 3. The fluid domain is updated at every increment in both cases, with and without follower forces, in order to make the flow field change softer, help and speed up the convergence of the aeroelastic system. The CFD solution is recomputed and if the follower forces feature is enabled the new load $L_k^{updated_{j+1}}$ will be sent to the service and used in Eq. 4, otherwise the aerodynamic load L_k will be employed to calculate the new load increment, Eq. 3.
Without follower forces, at the end of the exchange k, the load passed to the structure corresponds to 100% of the load L_k calculated on the fluid domain configuration as it is at the beginning of the exchange. With follower forces instead, it will be 100% of the load computed on the fluid domain updated N-times, $L_k^{updated_N}$.

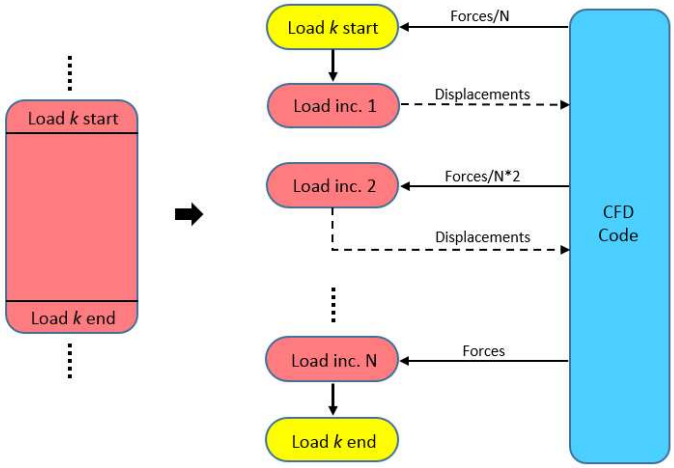

Fig. 3: Sub-cycling exchange

It is easy to see that if the incremental loads capability is employed lonely, the load will be given in increments, helping the convergence of both FEM and CFD models, but the load direction will not be changing during the sub-cycling and the magnitude will be simply an increasing percentage of the aerodynamic load calculated at the beginning of the exchange.
On the other hand, thanks to the follower forces approach, the load changes both in magnitude and direction at every iteration as the structure deforms and the steady-state configuration achieved would be more realistic. The more the structure is nonlinear the more this effect will be evident.

The number of increments N_k can be defined independently from one load exchange to another. More increments should be employed in the first loads, when the aerodynamic forces vary the most and the structure deforms highly, while it decreases in the last steps as the structure gets closer to the steady-state configuration.

The proposed SCA service manages how the FEM solver sends and receives data, defines coupling parameters (incremental loads, follower forces, number of exchanges, convergence criterions, transient explicit or implicit coupling, displacement predictor order..), handles the aerodynamic-structure interpolation data between FEM and CFD wetted surfaces and the fluid domain deformation based on the CFD wetted surface displacement.

On the CFD side, customized User Defined Functions (UDF), dynamically loaded with the SC/Tetra solver, have been developed to send and receive information (loads/displacement) from and to the SCA service, deforms the fluid domain, and check the CFD convergence.

2.3 Aero-structure grid interpolation

The 6DOF Spline technology, SPLINE6 (3D finite surface spline) and SPLINE7 (3D finite beam spline), have been specifically developed by MSC Software for structure to structure load mapping and for aero to structure load/displacement mapping and is available in static aeroelasticity solution SOL 144. For aeroelastic applications, both structural and CFD wetted surfaces must be defined in the FEM solver to build the interpolation spline matrix between the structural and aero wetted grids. Details of this technology will not be treated in this work since it is described in literature [3][9]. During the solution, the FEM solver creates the connections between the structural and aerodynamic nodes – only those ones defined in the wetted surfaces - and populates the transformation spline displacement matrix $[G_{KG}^{D}]$, to transform displacement from the structural grid (G-set) to the aerodynamic grid (K-set), Eq. (5), and the transformation spline load matrix $[G_{KG}^{P}]^{T}$, to transform forces from the aerodynamic grid to the structural grid, Eq. (6).

$$\{u_K\} = [G_{KG}^{D}]\{u_G\} \tag{5}$$

$$\{F_G\} = [G_{KG}^{P}]^{T}\{F_K\} \tag{6}$$

In the previous equations, $\{F_G\}$, $\{u_G\}$, $\{F_K\}$, $\{u_K\}$ are respectively force and displacement of the structural wetted nodes and force and displacement of the CFD wetted nodes.
It should be mentioned here that there is the option of having a separate spline matrix for force and displacement transformation. The algorithms used are identical in the two cases but the set of points used in the splining could be different. The rationale for allowing separate force and displacement splines that is appropriate for predicting aerodynamic displacement may not be good for applying forces.
For example, a grid point on a wing surface that is not attached to substructure may be needed to get a smooth pattern on the aerodynamic mesh may load the structure inappropriately if it is included in the force transformation.
Moreover, structural and aerodynamic points which constitute the wetted surfaces can be a sub-set of the models.

The linear beam model shown in Fig. 4 is used to illustrate the results of one CFD-FEM load/displacement exchange cycle of a fix-wing clamped at the root, obtained with the described interpolation procedure.

(a) CFD wetted surface (b) FEM model

Fig. 4: Fix wing model

The aerodynamic wetted surface has about 60000 nodes, Fig. 4 (a), while for the structure only 40 nodes that lie on the wing axis have been selected as the structural wetted surface. To better

visualize the bending and torsion of the wing under the loading, plot elements have been added and connected from the leading and trailing edges to the wing beam axis. SPLINE 7 has been used in this case.
The aero-structure interpolation technology ensures the energy equilibrium when the aerodynamic load is transferred to the structure in terms of forces and moments, Fig. 5.

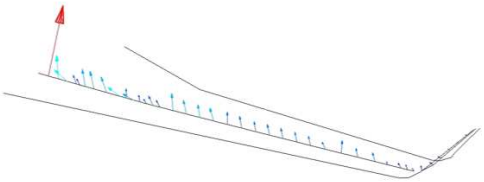

(a) FEM – Structural forces on wetted surface

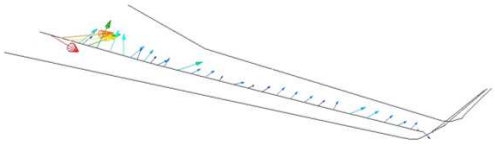

(b) FEM – Structural moments on wetted surface

Fig. 5: Fix wing model

To check the load transfer, the integrated structural and aerodynamic loads are calculated about a global coordinate system located at the FEM origin. Force and moment components (CX, CY, CZ, CMX, CMY, and CMZ) are the same for both wetted surfaces as it is shown in the column "RIGID AIR" reported in Fig. 6.

```
                    A E R O D Y N A M I C    M O N I T O R    P O I N T
                CONFIGURATION = AEROSG2D     XY-SYMMETRY = ASYMMETRIC
                              MACH = 9.000000E-01                Q =

CONTROLLER STATE:
LOADFACT =   1.0000E+00

MONITOR POINT NAME = AEROSG2D          COMPONENT =                    CLAS
LABEL = Full Vehicle Integrated Loads
 CP =      200          X =  0.00000E+00          Y =  0.00000E+00

  AXIS      RIGID AIR       ELASTIC REST.
  ----   -------------   -------------
   CX    -5.320223E+01   -5.320223E+01
   CY    -2.149361E+03   -2.149361E+03
   CZ     5.381967E+03    5.381967E+03
   CMX    1.289138E+06    1.289138E+06
   CMY    2.141187E+05    2.141187E+05
   CMZ   -1.117899E+03   -1.117899E+03
```

(a) Integrated load on CFD wetted surface

```
                    S T R U C T U R A L    M O N I T O R    P O I N T
                CONFIGURATION = AEROSG2D     XY-SYMMETRY = ASYMMETRIC
                              MACH = 9.000000E-01                Q

CONTROLLER STATE:
LOADFACT =   1.0000E+00

MONITOR POINT NAME = AEROSG2D          COMPONENT =                    CL
LABEL = Full Vehicle Integrated Loads
 CP =      200          X =  0.00000E+00          Y =  0.00000E+00

  AXIS      RIGID AIR       ELASTIC REST.   RIGID APPLIED    REST. APPL
  ----   -------------   -------------   -------------   ----------
   CX    -5.320223E+01   -5.320223E+01    0.000000E+00    0.000000E+
   CY    -2.149361E+03   -2.149361E+03    0.000000E+00    0.000000E+
   CZ     5.381967E+03    5.381967E+03    0.000000E+00    0.000000E+
   CMX    1.289138E+06    1.289138E+06    0.000000E+00    0.000000E+
   CMY    2.141187E+05    2.141187E+05    0.000000E+00    0.000000E+
   CMZ   -1.117904E+03   -1.117904E+03    0.000000E+00    0.000000E+
```

(b) Integrated load on the structure

Fig. 6: Integrated aerodynamic load about the global coordinate system

The structural displacement obtained based on the driving forces and moments, Fig. 7 (a), are interpolated back on the CFD wetted surface, Fig. 7 (b), and the aerodynamic shape achieved is regular and smooth.

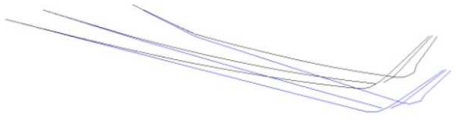

(a) FEM – structural displacement

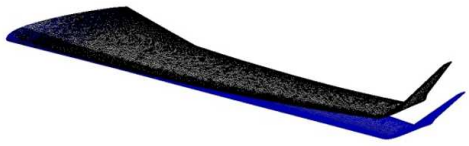

(b) CFD wetted surface - displacement

Fig. 7: Fix wing model

As far as the solution performance is concerned (SOL 144 is called at the initialization phase of the FSI analysis to create the spline matrices $[G_{KG}^{D}]$ and $[G_{KG}^{P}]^{T}$) and disk space needed to store the spline matrices (those ones are put in memory by the service in the initialization phase

of the FSI simulation) it has been proven that using several splines to connect the aerodynamic and structural wetted grids makes the FEM solver run much faster to populate the matrices and drastically reduces the disk space required to store those ones.
As the number of spline increases spanwise, Fig. 8 (a), the solution time and disk space decrease considerably, Fig. 8 (b) and Fig. 8 (c).

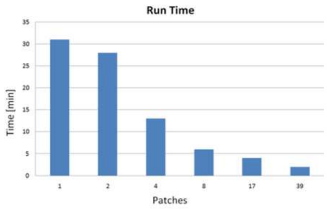

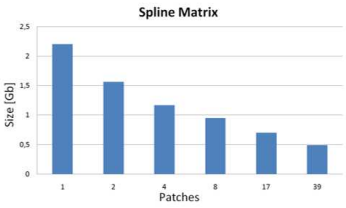

(a) CFD wetted surface splines (b) SOL 144 run time (c) Matrix disk space

Fig. 8: Fix wing model - scaling

The simulation presented has been run on an 8.0 Gb RAM, 1.87 GHz machine with 4 proc. The solution goes from about 32 minutes, when only one spline is employed, to about 40 seconds, with 39 splines (patches), whereas the spline matrix space from more than 2 Gb to less than 0.5 Gb (in this application the same spline matrix is used for both load and displacement transformations). The efficiency could have been further improved by creating multiple splines also chordwise, not done for this application.

A research grid algorithm has been developed to create multiple splines which ensures the continuity of the load and displacement patterns at the patches boundaries [2].
Furthermore, this procedure allows to better represent the aerodynamic load on the structure since the load is locally transferred instead of being spread over the structure and loose than the aerodynamic load pattern.

An aeroelastic model of a very thin rotating blade of MAV [5], Fig. 9, has been used to illustrate that aspect. The CFD model has hexahedral cells while the FEM model is represented via quadrilateral plate elements, Fig 10 (a).

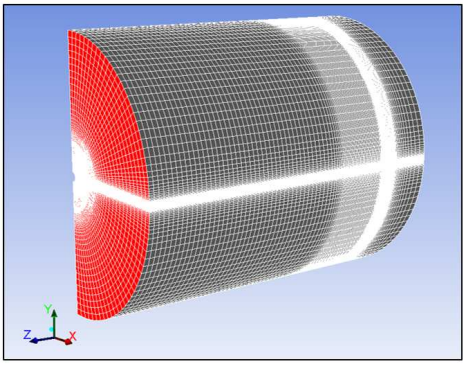

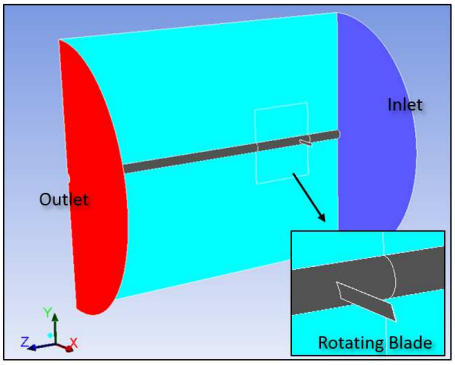

(a) CFD model – Fluid domain (b) CFD model – Boundary conditions

Fig. 9: CFD model of rotating blade of MAV

Multiple chordwise and spanwise splines have been created for this application, Fig. 10 (b).

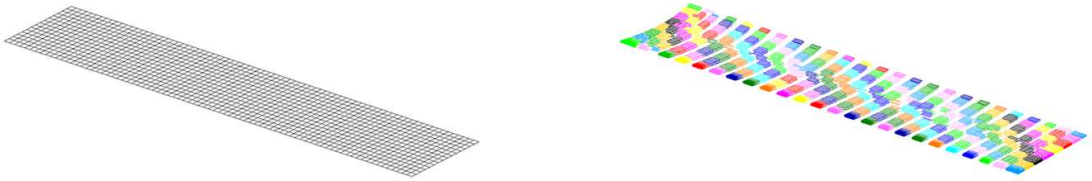

(a) FEM – 1200 CQUAD4, 1296 grids (b) CFD wetted surface – Splines, 14667 grids

Fig. 10: Blade FEM and CFD wetted surfaces

Only one load transfer has been performed from the CFD to the FEM model to illustrate the benefit of employing several splines. The aerodynamic load pattern, Fig. 11 (a), is accurately reproduced on the structural model, Fig. 11 (b).

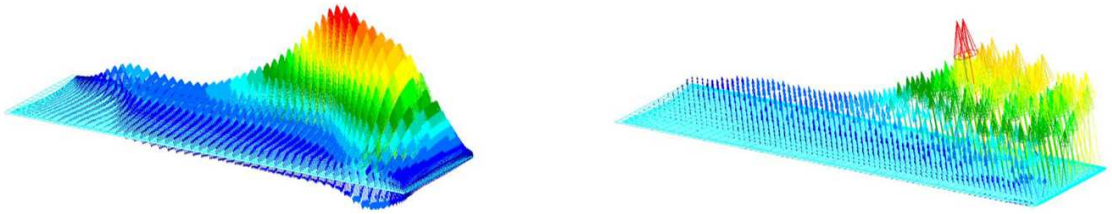

(a) CFD wetted surface – Aerodynamic forces (b) FEM wetted surface – Aerodynamic forces

Fig. 11: Aerodynamic forces on FEM and CFD wetted surfaces

2.4 Fluid domain deformation

SC/Tetra does not have a dynamic mesh tool to perform a fluid domain deformation during a fluid-structure interaction simulation. Here the need to develop an algorithm to carry out this task.

A linear Nastran-Based Interpolation Tool (NBIT) has been designed and incorporated in the proposed service to perform the fluid domain deformation based on the displacement computed on the CFD wetted surface with Eq. 5, at each load increment or time step, for a steady and transient simulation respectively.

An aeroelastic model of a flap in a duct is used to explain the developed procedure and results of a nonlinear steady-state FSI simulation will be presented in the next section.

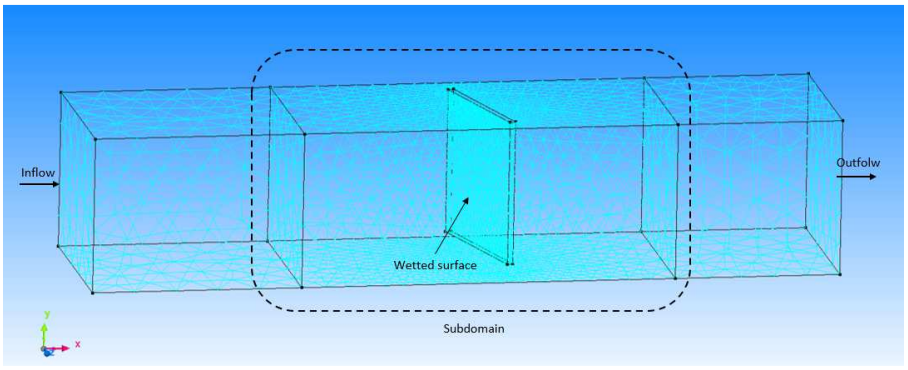

Fig. 12: Flap in a duct. CFD domain, boundary conditions and subdomain used to create the FEM_{CFD} model

The fluid domain or a subdomain of it that encapsulates the deformable wall, Fig. 12, is transformed into a linear Nastran FEM model, called FEM_{CFD}, Fig. 13. Specific UDF have been developed and loaded in the CFD code for that purpose.

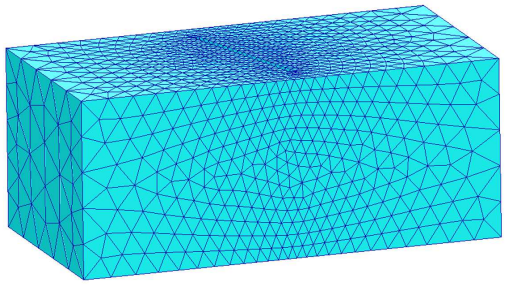

Fig. 13: Subdomain FEM_{CFD} model

At the beginning of the FSI simulation, before the FEM and CFD codes are called and start solving, the UDF loops over each fluid tetrahedral volume within the subdomain and creates a CTRIAR element for each volume's face, unless it exists already. Material and element properties are defined in order to have less element deformation close to the wetted surface and more as the nodes move from the deformable wall. Boundary conditions are imposed to the external boundaries of the subdomain by constraining to zero the out-of-plane displacement through SPC1 cards where nodes are allowed to move only in the plane. Dummy enforced displacement conditions $\{Y_S^D\}$ are applied on the nodes of the wetted surfaces by means of a combination of SPCD and SPC1 cards.
A linear static solution SOL 101 is performed and the $[K_{fs}]$ and $[LLL]$ matrices are extracted by means of a DMAP alter [10] and read by the service. The matrix $[K_{fs}]$ is the partitioned stiffness matrix that allows to reduce the static load vector $\{P_f\}$ on free nodes (where no SPC1 and SPCD condition are applied) from the enforced displacement vector $\{Y_S\}$ as following:

$$\{P_f\} = -[K_{fs}]\{Y_S\} \tag{7}$$

In the previous equation, the enforced displacement vector $\{Y_S\}$ contains the aerodynamic displacement $\{u_K\}$ computed on the CFD wetted surface during the simulation with eq. 5 and the components of constrained nodes on the external boundaries.
In other words, $\{P_f\}$ is the structural load should be applied to the free nodes of the FEM_{CFD} model to obtain the same solution when enforcing the displacement on the wetted surface and constraining the external boundaries.

The matrix $[LLL]$ is the lower triangular factor/diagonal matrix from $[K_{LL}]$ that is the stiffness matrix of the FEM_{CFD} model. The advantages of using $[LLL]$ are that $[LLL]$ is a sparse factor matrix, that allows to save a lot of disk space, and the linear problem to be solved to recover the grid displacement of the subdomain, Eq. 8, can be rewritten as Eq. 9:

$$[K_{LL}]\{X\} = \{P_f\} \tag{8}$$

$$[LLL][D][LLL]^T\{X\} = \{P_f\} \tag{9}$$

Where $[D]$, $[LLL]^T$, and $\{X\}$ are respectively the diagonal matrix, the upper triangular factor matrix from $[K_{LL}]$ and the solution of the problem, the displacement of the free nodes of the FEM_{CFD} model.
The solution $\{X\}$ in Eq. 9 can then be simply computed through a Forward-Backward Substitution (FBS) procedure by solving for $\{Y\}$ first, Eq. 10, and then Eq. 11:

$$[LLL]\{Y\} = \{P_f\} \tag{10}$$

$$[D][LLL]^T\{X\} = \{Y\} \tag{11}$$

Eq. 10 and Eq. 11 are respectively the forward substitution and the backward substitution.

The solution of the FEM_{CFD} model is then composed by the displacement $\{X\}$ and the enforced displacement on the wetted surface $\{u_k\}$ than changes at each FEM-CFD exchange, and external boundaries constraints that usually do not vary during the FSI simulation, Fig. 14.

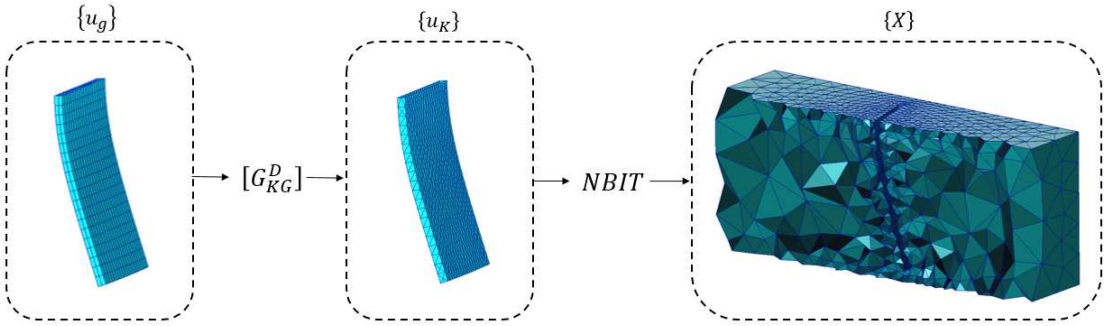

Fig. 14: NBIT workflow developed in the service - FEM_{CFD} deformation

The CFD solver reads from the service the new positions of the aerodynamic nodes calculated by the NBIT module and deforms the fluid domain through UDF, Fig. 15.

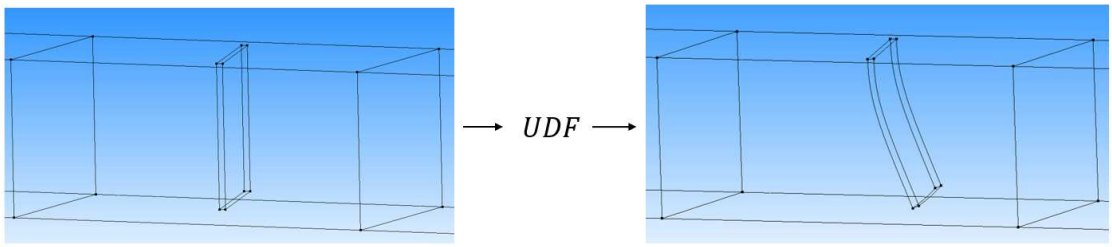

(a) CFD domain – before deformation (b) CFD domain after deformation

Fig. 15: Fluid domain deformation – NBIT workflow developed in the service

3 NUMERICAL RESULTS

Analyses to assess the developed nonlinear steady-state FSI procedure are discussed in Sec. 3.1. The proposed methodology is then applied to a rotating propeller two-blade model of MAV [5] in Sec. 3.2.

3.1 Test case 1 – Flap in a duct

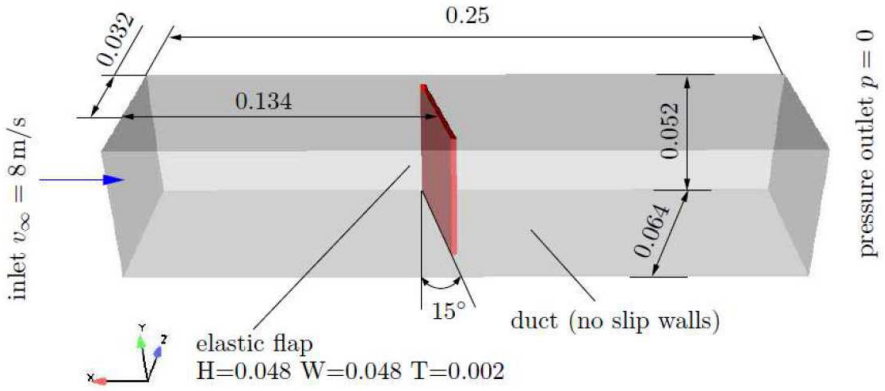

Fig. 16: Elastic flap in duct: Geometry (meters) and boundary conditions

The developed steady-state tool is assessed by computing the nonlinear response of a clamped flap in a duct at prescribed free-stream velocity and angle between the flap and flow direction, Fig. 16 [4]. Results will be compared with the steady-state deformation obtained through nonlinear explicit transient FSI analysis in Sec. 3.1.2.

The material of the structure has a density value of ρ = 1000 kg/m3, elastic modulus E = 1.0×10e8 Pa and Poisson's ratio ν = 0.49. The FEM model consists of 800 solid elements CHEXA with 8 nodes each. The FEM model is clamped on the top where translational displacement are constraint to zero. Large displacement have been enabled, Fig.17.

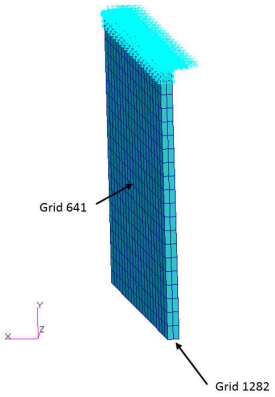

Fig. 17: FEM solid model

The CFD model, already shown in Sec. 2.4 is composed of 24811 tetrahedral cells with boundary conditions shown in Fig. 16. Ideal gas for the air, energy activated and pressure-based solver used to calculate the solution. The standard $k-\varepsilon$ model has been chosen for the viscous model.

3.1.1 Nonlinear static FSI simulation

For this application the nonlinear solver has been set to static while the CFD code to steady. The main convergence criteria parameters for the structural solution (the error tolerance for displacement EPSU, residual load EPSP, and work EPSW and the number of iteration within

each structural load increment allowed before bisection NINC) have been kept as for the default values, Tab 1. The convergence absolute criteria for the CFD simulation are listed in Tab. 2.

EPSU	EPSP	EPSW	NINC
-1.E-01	1.E-01	1.E-01	25

Table 1: Nastran convergence criteria parameters

Continuity	Velocity	Energy	k	ε
1.E-4	1.E-4	1.E-6	1.E-4	1.E-4

Table 2: CFD convergence absolute criteria

The CFD solution convergence has been achieved before starting the FSI simulation, Fig. 18.

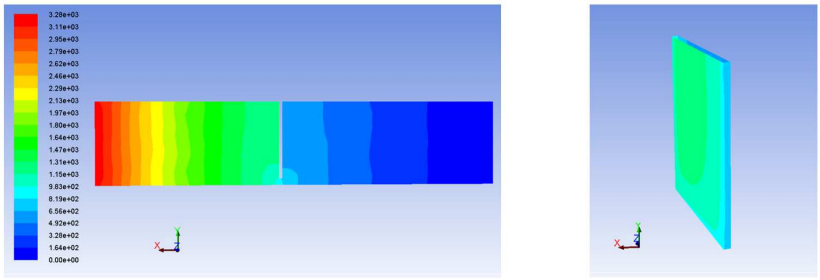

Fig. 18: Converged CFD steady simulation – Static pressure (Pascal) in the fluid domain and on the flap

Five CFD-FEM exchanges are defined for the analysis with incremental loads and follower forces. At the end of the steady-state simulation, after 25 load/displacement iterations, the flap tip x-displacement read at the grid 1282 is reported in Tab 3.

N. of Exchanges	N. of Sub-cycles	Incr. loads	Foll. forces	$\bar{u}_{x_{1282}}$(m)
5	5	Yes	Yes	-0.494030E-2

Table 3: CFD-FEM coupling parameters and flap tip x-displacement

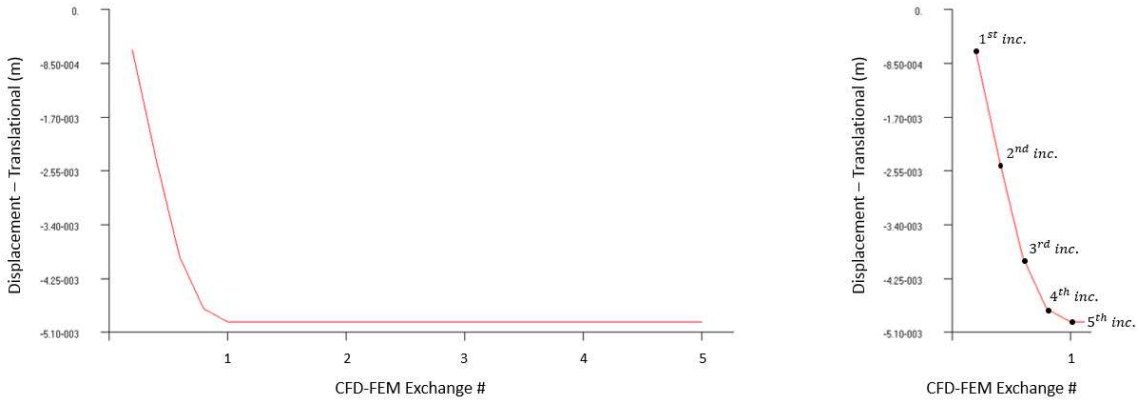

(a) Tip displacement after 5 exchanges – 25 iterations (b) Sub-cycling within 1st exchange

Fig. 19: Displacement convergence - Node 1282 x-displacement vs FEM-CFD exchanges

At the end of the first exchange the aeroelastic system has almost converged, Fig. 19 (a). The steady-state deformation achieved and the aeroelastic forces are shown in Fig. 20.

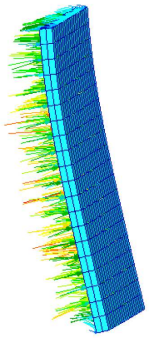

Fig. 20: FEM model – Steady-state deformation and aeroelastic load

The aerodynamic load stabilizes after a few iterations as the displacement does. The force components (FX, FY, and FZ) read on the grid 641 are shown in Fig 20.

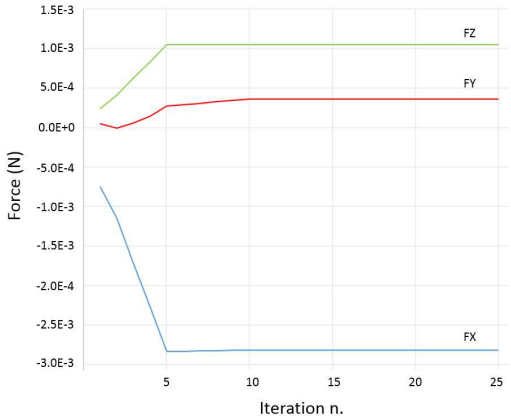

Fig. 20: Load convergence – Force components on grid 641

The aerodynamic load follows the structure as it deforms thanks to the follower forces feature. During the five iterations within the first load exchange L_1, Fig. 19 (b), the aerodynamic load sent to the FEM solver, $Load_1\ inc_j$, calculated with Eq. 4, updates both magnitude and direction because the fluid domain is updated and solution recomputed at every iteration, Fig. 21.

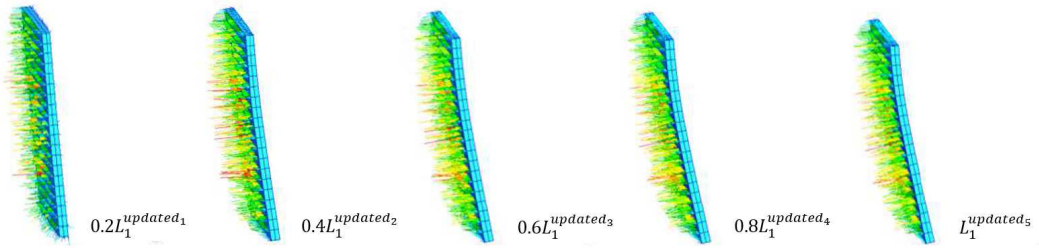

Fig. 21: Aerodynamic load on the flexible structure within the first exchange – Follower forces

Contrary, the aerodynamic load on the structure would keep the same direction without employing follower forces as it is qualitatively illustrated in Fig. 22.

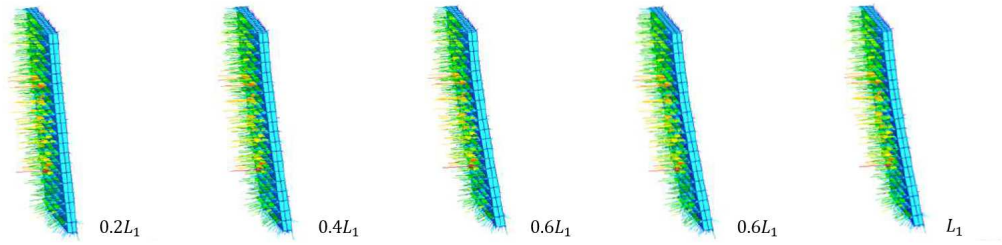

Fig. 22: Aerodynamic load on the flexible structure within the first exchange – No follower forces

3.1.2 Nonlinear transient FSI simulation

For the transient FSI simulation the nonlinear solver has been set to transient while the CFD code to unsteady.
Conventional Serial Staggered (CSS) explicit and implicit coupling strategies are available in the developed SCA service, Fig. 23.

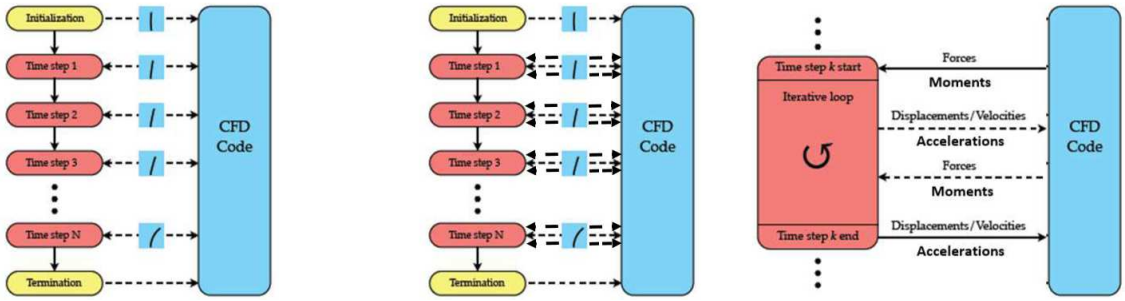

(a) Explicit coupling (b) Implicit coupling

Fig. 23: Transient coupling workflow strategies

For this test case, the explicit coupling strategy has been used. Zero, first and second displacement predictor order schemes have been employed to predict the aerodynamic displacement from the structural solver.

$$\bar{u}_k^{t+1} = \bar{u}_k^t + 0.5\Delta t * \bar{v}_k^t \tag{12}$$

$$\bar{u}_k^{t+1} = \bar{u}_k^t + 1.0\Delta t * \bar{v}_k^t + 0.5\Delta t(\bar{v}_k^t - \bar{v}_k^{t-1}) \tag{13}$$

In the previous equations, respectively first and second displacement predictor orders, $\bar{u}_k^{t+1}$and $\bar{u}_k^t$ are the aerodynamic displacement computed on the CFD wetted surfaces through Eq. 5 at time *t+1* and time *t*; $\bar{v}_k^t$ and $\bar{v}_k^{t-1}$ are the velocities calculated on the CFD wetted surface at time *t* and time *t-1* with Eq. 14, where $\bar{v}_G^t$ is the velocity of the structural wetted surface and $\bar{\bar{G}}_{KG}^D$ the displacement spline matrix; Δt is the solution time step.

$$\bar{v}_k^t = \bar{\bar{G}}_{KG}^D \bar{v}_G^t \tag{14}$$

For the flap model the simulation time step of 0.00025s is fixed for both FEM and CFD solvers with a simulation time of 0.2s. Large displacement are activated.
The flap stabilizes faster in the case with the first and second displacement predictor orders, Fig. 24.

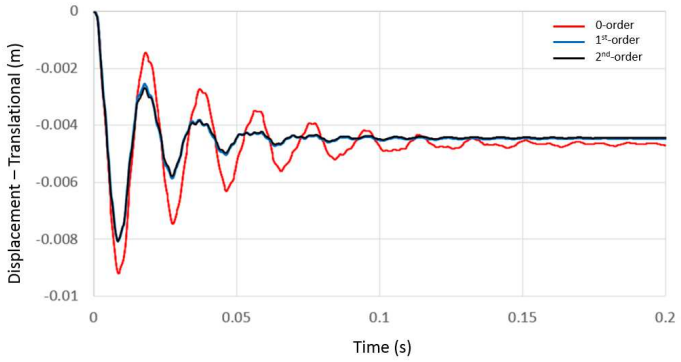

Fig. 24: Displacement convergence - X-displacement time history of node 1282

Comparisons of the steady-state displacement read on the node 1282 between the transient simulations and the steady-state approach, with elapsed simulation run time, are shown in Tab. 4.

	0 – Tran.	1st – Tran.	2nd – Tran.	Steady
$\bar{u}_{x_{1282}}$(m)	-0.47225E-2	-0.44356E-2	-0.44035E-2	-0.49403E-2
Run time (min)	76	76	76	11

Table 4: Flap tip x-displacement – Transient vs steady

For this aeroelastic model, results are available from other transient coupling strategies performed between different FEM codes and the Fluent solver with zero displacement predictor order scheme [4], Fig. 25. All the simulations lead to a flap tip displacement steady-state value that is between -0.46E-2m and -0.49E-2m, in agreement to the present study.

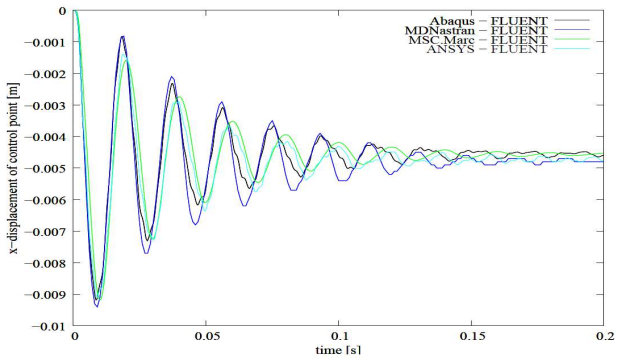

Fig. 25: Elastic flap - X-displacement time history of node 1282

Results achieved by the steady-state approach proposed in Sec. 3.1.1 are in good agreement with the transient simulations, especially those ones conducted with the zero order displacement predictor scheme, probably because the velocity is not considered to predict the displacement. The novel methodology allows to reduce the simulation run time by a factor of 7.

3.2 Test case 2 – Graupner8” × 6” propeller model

For the propeller model Graupner 8"x6" [5] two different CFD domains were used. The first domain refers to the stationary control volume and the second refers to a rotating control volume at 5000rpm. The propeller model was put inside the rotating volume and at the same time this rotating domain was located at the center of the static domain.
Both stationary and rotating domains use fully unstructured prismatic mesh. A decahedron shape was chosen for stationary computational domain. The surfaces of the decahedron were grouped in two opposite flat top pyramids to be used as inlet and outlet boundaries, Fig. 26.

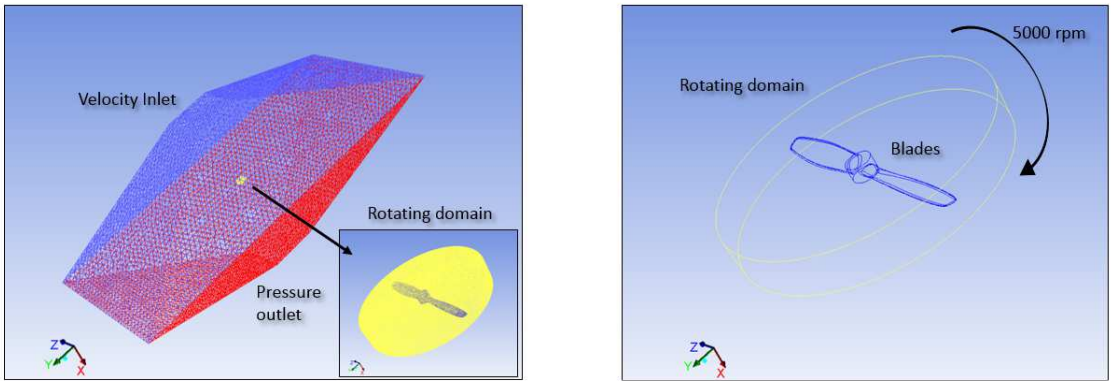

(a) Boundary conditions (b) Rotating domain and propeller model

Fig. 26: Computational fluid domain

The size of the total grid of this model is 11.09 million. The CFD wetted surfaces has 232855 points, Fig 27 (b).

(a) FEM model (b) CFD wetted surface

Fig. 27: Propeller model – Structural and CFD wetted surfaces

The structural model is made by 50 2-node beam elements per blade, with a half spam of 0.0894m, with lagrangian formulation activated to allow for geometric nonlinearities. The structural wetted surface has 102 grids, Fig 27 (a).

(a) 20 spl. – Spanwise (b) 80 spl. – Spanwise (c) 308 spl. Spanwise/Chordwise

Fig. 28: Spline configurations

For this test case, because the number of the aerodynamic points is quite huge, several spline configurations have been investigated in order to reduce as much as possible the time took by the process to create the aero-structure interpolation matrix and the space needed to store the spline matrices. Both spanwise and spinewise/chordwise patches have been tested, Fig 28.
The size of the spline matrix and run time obtained with the different spline configurations are reported in Tab. 5. Having different spline matrices for force and displacement transformations (F/D) makes the solution run slower than having one spline for both (Both).

Configuration n.	1st	2nd	3rd	4th	5th	6th	7th	8th	9th
N. of splines	1	20	20	80	80	200	200	308	308
Spline type	Both	F/D	Both	F/D	Both	F/D	Both	F/D	Both
Spline size (Gb)	12.36	3.54	2.38	1.04	0.52	0.56	0.28	0.43	0.22
Run time (min)	151.0	22.5	12.5	6.2	3.1	3.0	1.5	1.5	0.9

Table 5: SOL 144 run time

The size of the spline goes from more than 12.0 Gb in the 1st configuration with only one spline employed for both transformations, to about 0.22 Gb in the 9th configuration with 308 patches supplied for both transformations. The simulation run time moves from more than two hours to less than one minute.
The 7th spline configuration has been retained for the FSI application since it has been found a good compromise between performances and the quality of the load/displacement interpolation.
The first load exchange performed at the initialization phase is illustrated in Fig. 29.

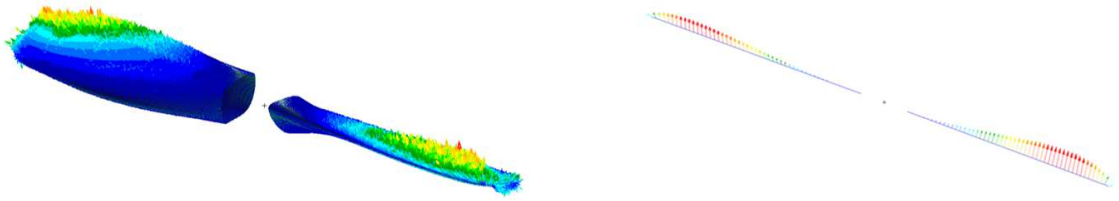

(a) CFD wetted surface – Aerodynamic forces (b) FEM wetted surface – Aerodynamic forces

Fig. 29: Aerodynamic forces on FEM and CFD wetted surfaces at the initialization phase

Integrated monitor points are employed to verify the energy equilibrium when the first load is transferred to the structure, Fig 30. The six components of the load (CX, CY, CZ, CMZ, CMY, and CMZ) computed about the global coordinate system located at the origin of the FEM model read the same values for both the aerodynamic and structural wetted surfaces.

```
                    A E R O D Y N A M I C   M O N I T O R
                CONFIGURATION = RAERO        XY-SYMMETRY =


CONTROLLER STATE:
URDD3     =   1.0000E+00

MONITOR POINT NAME = RAERO              COMPONENT =
LABEL = Full Vehicle Integrated Loads
 CP =         0          X =  0.00000E+00          Y =  0.000

  AXIS      RIGID AIR       ELASTIC REST.
  ----    -------------     -------------
   CX    -1.356991E+00     -1.356991E+00
   CY     6.925236E-04      6.925236E-04
   CZ     8.761848E-05      8.761848E-05
   CMX   -2.813419E-02     -2.813419E-02
   CMY   -1.017996E-04     -1.017996E-04
   CMZ   -2.121593E-06     -2.121593E-06
```

(a) Integrated load on CFD wetted surface

```
                    S T R U C T U R A L   M O N I T O R
                CONFIGURATION = RAERO        XY-SYMMETRY =


CONTROLLER STATE:
URDD3     =   1.0000E+00

MONITOR POINT NAME = RAERO              COMPONENT =
LABEL = Full Vehicle Integrated Loads
 CP =         0          X =  0.00000E+00          Y =  0.00

  AXIS      RIGID AIR       ELASTIC REST.    RIGID APPLIED
  ----    -------------     -------------    -------------
   CX    -1.356991E+00     -1.356991E+00     0.000000E+00
   CY     6.925235E-04      6.925235E-04     0.000000E+00
   CZ     8.761847E-05      8.761847E-05     0.000000E+00
   CMX   -2.813419E-02     -2.813419E-02     0.000000E+00
   CMY   -1.017996E-04     -1.017996E-04     0.000000E+00
   CMZ   -2.121593E-06     -2.121593E-06     0.000000E+00
```

(b) Integrated load on the structure

Fig. 30: Integrated aerodynamic load about the global coordinate system

The load check is carried out at each iteration by the service to evaluate whether some energy is added to the system or rather removed from it.

Five CFD-FEM exchanges are defined for the FSI steady-state analysis with different sub-cycles within each step as reported in Tab. 6.

N. of Exchanges	N. of Sub-cycles	Incr. loads	Foll. forces	$\bar{u}_{x_{tip}}$(m)
5	10/5/5/5/5	Yes	Yes	-0.0193

Table 6: CFD-FEM coupling parameters and blade tip x-displacement

At the end of the 3rd exchange the aeroelastic system has already converged to the steady-state deformation, Fig. 31.

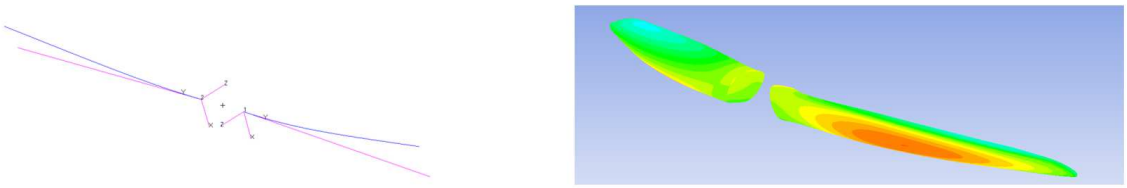

(a) FEM model – Steady-state deformation (b) CFD wetted surface and static pressure

Fig. 31: Propeller MAV model – Steady-state deformation and aeroelastic load

In this application the static loading condition due to the angular velocity of the blades has been considered in the FEM solver on top of the aerodynamic load.

4 CONCLUDING REMARKS

A novel approach has been presented to allow for accurate nonlinear steady-state FSI simulations for highly flexible structures. The new main features developed in the methodology are: a SCA service to enable the communication between the Nastran solver and SC/Tetra code and perform the interpolation data between dissimilar grids through 6DOF spline technology; spline capabilities to reduce the simulation time needed to create the aero-structure interpolation matrix, cut down the disk space required to store the spline matrix and improve the quality of the load transfer; follower forces and incremental loads features to better describe the physics of the coupling and help the convergence of both structural and CFD solvers; a FEM-based interpolation algorithm to handle the fluid domain deformation implemented directly in the service.
The methodology has been validated on a flap in a duct model where results from transient FSI simulations were available. The proposed steady-state approach is in good agreement with results obtained via transient FSI analysis performed through CSS explicit coupling strategies accessible in the developed service with certain displacement predictor order schemes, and with other results available in literature. The methodology has been then applied to a propeller two-blade model of MAV from ISAE. The new spline features allowed reducing tremendously both memory requirements and simulation time needed for spline generation without compromising the quality of results and the energy equilibrium. Future work will address the proposed approach to the prediction of the nonlinear steady-state response of a highly flexible two-bladed rotor with rectangular plan-form from ISAE where experimental results are available [11]. One

of the potential extension of the presented approach is to couple the steady-state analysis with 3D rotordynamics.

5 REFERENCES

[1] MSC.Software Corp., 2 MacArthur Place, Santa Ana, CA 92707, USA, “MSC Nastran 2014 - Non Linear User’s Guide SOL400”, 2014.

[2] F. G. Di Vincenzo, A. Castrichini, MSC Software Corp., Toulouse, 4 Rue du Professeur Pierre Vellas, France, “Hybrid Static Aeroelasticity Toolkit”, 2013.

[3] MSC.Software Corp., 2 MacArthur Place, Santa Ana, CA 92707, USA, “MD Nastran 2006 Release Guide”, 2006.

[4] Fraunhofer Institute for Algorithms and Scientific Computing SCAI, Schloss Birlinghoven, 53754 Sankt Augustin, Germany “MpCCI 4.4.1-1 Documentation, Part I,” 2015.

[5] F. M. Zawawi, ISAE SUPAERO-CNRS-INSA-Mines Albi-UPS, “Aeroelastic Analysis of Flexible Composite Proprotor Blades for Convertible Micro Air Vehicles”, France 2014.

[6] Farhat, C., & Lesoinne, M. (2000). Two efficient staggered algorithms for the serial and parallel solution of three-dimensional nonlinear transient aeroelastic problems. Computer methods in applied mechanics and engineering, 182(3), 499-515.

[7] Dowell, E., Edwards, J., & Strganac, T. (2003). Nonlinear aeroelasticity. Journal of aircraft, 40(5), 857-874.

[8] MSC.Software SOSP-73.13, “MSC Simulation Component Architecture Build System Guide”.

[9] MSC.Software Corp., 2 MacArthur Place, Santa Ana, CA 92707, USA, “Aeroelastic Analysis User’s Guide”, 2016.

[10] MSC.Software Corp., 2 MacArthur Place, Santa Ana, CA 92707, USA, “DMAP Programmer’s Guide”, 2017.

[11] Peng LV, ISAE SUPAERO-CNRS-INSA-Mines Albi-UPS, “Aerodynamic and Structural Performance of Flexible Blades for MAVs”, 2014.

COPYRIGHT STATEMENT